Determination of the molecular reach of the protein tyrosine phosphatase SHP-1

Lara Clemens[1*], Mikhail Kutuzov[2*], Kristina Viktoria Bayer[2], Jesse Goyette[3,4], Jun Allard[1¶], Omer Dushek[2¶]

[1]Center for Complex Biological Systems, University of California Irvine, Irvine, CA 92697 USA
[2]Sir William Dunn School of Pathology, University of Oxford, OX1 3RE, Oxford, UK
[3]EMBL Australia Node in Single Molecule Science, School of Medical Sciences, University of New South Wales, Sydney 2052, Australia
[4]ARC Centre of Excellence in Advanced Molecular Imaging, University of New South Wales, Sydney 2052, Australia
[*]These authors contributed equally
[¶]Co-Corresponding authors

Abstract

Immune receptor signalling proceeds by the binding of enzymes to their cytoplasmic tails before they catalyse reactions on substrates within reach. Studies of binding and catalysis have led to a binding-induced allosteric activation model for enzymes, such as SHP-1, whose catalytic activity increases upon recruitment to inhibitory receptors, such as PD-1. However, the impact of molecular reach is poorly understood. Here, we use surface plasmon resonance to measure binding, catalysis, and molecular reach for tethered SHP-1 reactions. We find a molecular reach for SHP-1 (13.0 nm) that is smaller than a maximum stretch estimate (20.4 nm) but larger than an estimate from crystal structure of the active conformation (5.3 nm), suggesting that SHP-1 explores a spectrum of active conformations. The molecular reach confines SHP-1 to a small membrane-proximal volume near its substrates leading membrane recruitment to increase its activity by a 1000-fold increase in concentration with a smaller 2-fold activity increase by PD-1 binding-induced allostery. Lastly, we use mathematical modelling to quantify the degree of co-clustering required for PD-1—SHP-1 complexes to reach their substrates.

Introduction

The initiation, maintenance, and termination of immune responses is tightly controlled to confer effective immunity to infected tissues without excessive collateral damage. These responses are controlled by the activation of immune cells, which itself is controlled by a balance of phosphorylation and dephosphorylation reactions from activating and inhibiting immune receptors (1, 2). These immune receptors are non-catalytic and contain unstructured cytoplasmic tails with conserved tyrosines (3). Ligand binding induces phosphorylation of these tyrosines, generating docking sites for the SH2 domains of kinases and phosphatases that in turn act on a variety of substrates to integrate their signals. For example, ligand binding to the immune inhibitory checkpoints PD-1 and BTLA in T cells induces phosphorylation on conserved immunoreceptor tyrosine-based inhibition (ITIM) and switch (ITSM) motifs (1, 4). These phosphorylated motifs recruit the protein tyrosine phosphatases SHP-1 and SHP-2, which are known to dephosphorylate activating tyrosines on the T cell receptor and the co-stimulatory receptor CD28 (5–8) (Fig. 1A). A dominant hypothesis for the control of SHP-1 and SHP-2 activity is allosteric activation, whereby these enzymes are inactive in the cytoplasm but increase their catalytic activity when their SH2 domains are engaged at the membrane (9–14).

In addition to being activated, these tethered enzymes must reach their substrates, which are often other surface receptors (12, 15, 16). Therefore, the efficacy of these reactions is controlled not only by the binding affinity to the receptor and the substrate catalytic rate, but also by the molecular reach of the reaction (L in Fig. 1A). This parameter sets the length scale determining how close receptors must be in order for their tethered-enzymes to catalyse reactions, and serves to confine the enzyme and substrate to small membrane-proximal volumes that can increase the local concentration (to approximately $\sigma^* = 1/L^3$) and thus the reaction rates (12, 16–18). Interestingly, many surface receptors on leukocytes form micro- and nano-clusters that co-localise receptors (5, 19–26), suggesting that cluster formation may be required for receptors to reach each other. This has been termed receptor-proximal signal integration (3).

The molecular reach of these reactions is presently unknown. There are three molecules that contribute to the reach: the receptor tail, the enzyme, and the substrate (16). Structural studies are challenging due to the presence of unstructured, disorder regions in these molecules. Theoretical estimates from the worm-like chain model and other polymer models have been used successfully to model reach for unstructured polypeptide chains based on the contour (l_c) and persistence (l_p) lengths as $L_{\text{peptide}} = (l_c l_p)^{1/2}$ (17). This theoretical approach would predict a reach of $L_{\text{PD-1}} = 3.0\,\text{nm}$ for the ITSM of PD-1 located 55 amino acids from the membrane ($l_c = 55 \times 0.4$ nm, where each amino acid contributes 0.4 nm to the contour length and l_p = 0.4 nm for random amino acid sequences (17, 27)). In the absence of other contributions, this short reach implies that surface receptors must come into (or nearly into) contact to enable reactions.

However, multi-domain enzymes such as SHP-1 may significantly contribute to this reach. SHP-1 binds phosphorylated tyrosines in receptor tails with its dominant N-terminal SH2 domain and catalyses reactions with a C-terminus protein tyrosine phosphatase (PTP) domain (9, 10, 12) as shown in Fig. 1A. Based on the crystal structure of the open active conformation of SHP-1 (28), the reach between the N-SH2 and the catalytic pocket is estimated to be $5.3\,\text{nm}$. Alternatively, we can estimate reach by assuming that the linkers between the SH2 domains and between the C-terminal SH2 and PTP domain are maximally stretched, as in Fig. 1B, obtaining a reach of $20.4\,\text{nm}$. It may be the case that SHP-1 explores a range of conformations dynamically. Although these theoretical calculations can provide a starting estimate, other factors like the specific sequence of the unstructured region, interactions between domains, and the orientation of the enzyme relative to the substrate further complicate theoretical estimates (15).

Here, we extend our previously described surface plasmon resonance (SPR) based assay (12) to deter-

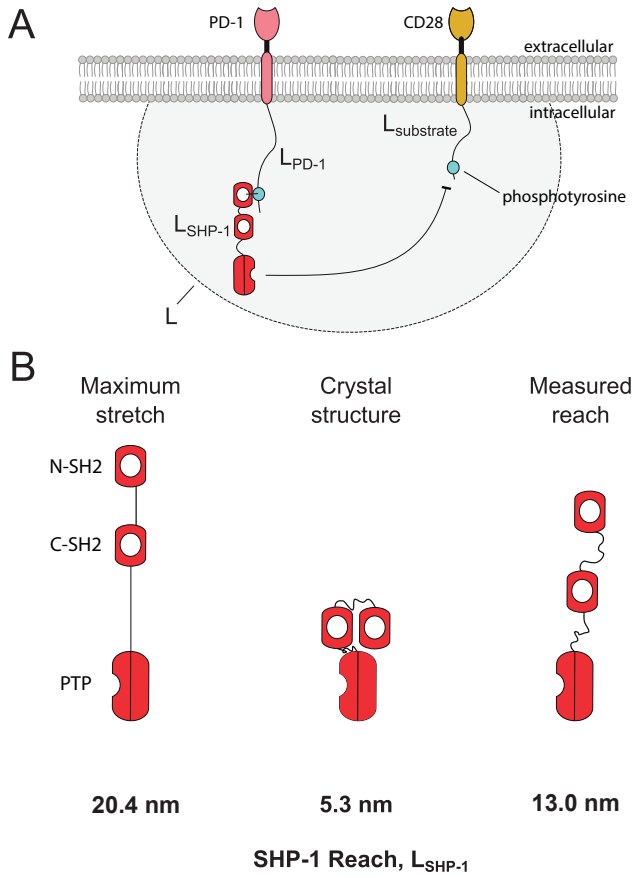

Figure 1: **Estimates of the molecular reach of SHP-1.** (A) Schematic of a tethered dephosphorylation reaction mediated by the tyrosine phosphatase SHP-1 (red) recruited to the membrane by the inhibitory receptor PD-1 (pink) acting to dephosphorylate the co-stimulatory receptor CD28 (orange). The molecular reach of the reaction, L (gray area), is determined by the molecular reach of PD-1 ($L_{\mathrm{PD-1}}$), CD28 (L_{CD28}), and SHP-1 ($L_{\mathrm{SHP-1}}$). (B) Estimates of SHP-1 molecular reach ($L_{\mathrm{SHP-1}}$) based on sequence, crystal structure, and experimental measurement in the present work.

mine the molecular reach of SHP-1 and PD-1 at 37°C. By systematically reducing the tether length, we isolate the molecular reach of SHP-1 from that of the PD-1 tether, finding a reach of 13.0 nm for SHP-1 and a reach of 6.55 nm for PD-1. To explore the implications of these parameters, we calculate the effective concentration of SHP-1 and its surface coverage (i.e. the fraction of substrate molecules within reach able to experience the effective concentration). We find that if PD-1 is uniformly distributed, SHP-1 achieves a membrane concentration that is 1000-fold higher than the cytoplasmic concentration but coverage is low, with only $\sim 10\%$ of substrates within reach. Clustering of PD-1 so that the density is 10-fold higher increases coverage to 90%. The work highlights the role of molecular reach in controlling surface receptor reactions and underlines the importance of surface receptor co-clustering.

Results

Extended SPR assay determines biophysical parameters for tethered reactions by SHP-1

We previously described an SPR-based assay and fitting procedure for extracting biophysical parameters of tethered reactions (12) (Fig. 2A). In that assay, murine SHP-1 was injected over initially phosphorylated ITIM peptide from murine LAIR-1 coupled to polyethylene glycol (PEG) repeats at 10°C and binding of SHP-1 (via its SH2 domains) is monitored by SPR over time. Since SH2 domains bind phosphorylated peptides, it was observed that although binding initially increases, it eventually decreases over the injection time because of peptide tether dephosphorylation via both tethered reaction (when SHP-1 is bound to the tether at the surface and acting on another tether) and solution reaction (when SHP-1 directly acts on a surface tether from solution without binding to a tether). The resulting multiphasic SPR traces were fit by a partial-differential-equation mathematical model describing multi-particle densities (MPDPDE model) including densities, spatial auto-correlation, and pair-correlations between tethers.

Here, we focus on human SHP-1 interacting with a phosphorylated ITSM peptide from human PD-1 initially coupled to 28 repeats of PEG (PEG28-PD1) and data is collected for different injected SHP-1 and immobilised PEG28-PD-1 concentrations at 37°C (Fig. 2). In contrast to our previous experiments (12), we noted a difference in the baseline SPR signal between the start at 0 seconds and the end at 45 seconds of the SHP-1 injection, for example visible in Fig. 2B,C. Using alkaline phosphatase, we found that this difference is not a result of phosphate mass being lost from the surface by dephosphorylation (Fig. S1) but can be explained by nonspecific binding of the enzyme (Fig. S2). We therefore extended our previous MPDPDE model to capture nonspecific binding by including three additional parameters (p_{start}, p_{stop}, p_{nsb}), see Methods for details.

We find that this extended eight-parameter MPDPDE model (k_{on}, k_{off}, $k_{\text{cat}}(\text{tethered})$, σ^*, $k_{\text{cat}}(\text{solution})$, p_{start}, p_{stop}, p_{nsb}) closely fits the SPR data (Fig. 2A-C). We perform Markov Chain Monte Carlo analysis to assess if the parameters can be uniquely identified and find this to be the case (Fig. S3). For each SPR trace, we use this extended MPDPDE model to extract all eight parameters, including the molecular reach (or, equivalently, the local concentration $\sigma^* = 1/L^3$).

Biophysical parameters associated with catalysis are independent of experimental conditions

We next verified that the biophysical parameters can be identified independently of experimental variables, specifically the SHP-1 and PEG28-PD-1 concentrations (Fig. 2D). We plot each fitted biophysical parameter as a function of the experimental variables finding that parameters associated with catalysis ($k_{\text{cat}}(\text{tethered})$, $k_{\text{cat}}(\text{solution})$, σ^*) are independent of these variables (correlations are not significant). In contrast, the binding parameters (k_{on}, k_{off}, and $K_{\text{D}} = k_{\text{off}}/k_{\text{on}}$) exhibited a correlation with SHP-1 concentration, with a statistically significant correlation for k_{on} and K_{D} after a correction for multiple hypotheses is implemented (indicated by red asterisks in Fig. 2D). A possible explanation for this correlation could be that higher concentrations of SHP-1 lead to steric crowding effects on the surface, whereby volume exclusion reduces the ability for more SHP-1 molecules to bind to the surface reducing apparent binding. Based on these results, we conclude that the SPR assay and subsequent model fitting procedure can be used to determine the molecular reach of the reaction independent of the SHP-1 and the immobilised peptide concentrations.

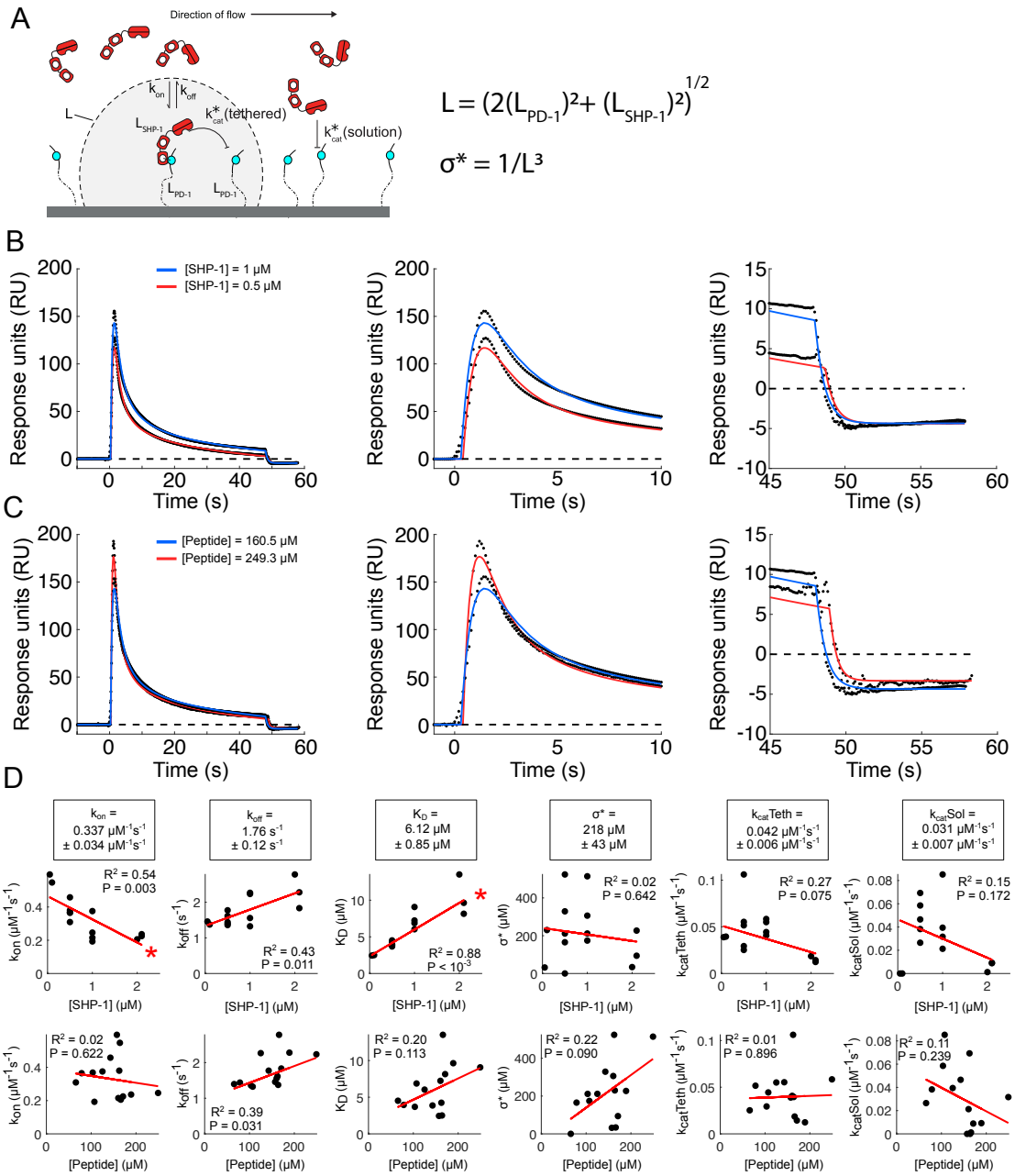

Figure 2: **Extended SPR-based assay for tethered catalytic reactions can recover biophysical parameters independent of experimental conditions at 37°C.** (A) Schematic of the SPR assay where SHP-1 (analyte) is injected over immobilised phosphorylated PEG28-PD-1 peptides. (B,C) Representative SPR traces (black dots) and MPDPDE model fit (solid lines) for two representative (B) injected human SHP-1 concentrations and (C) two immobilised PEG28-PD-1 concentrations. Middle and right panels show early and late time data, respectively. (D) Fitted parameters (black dots) against SHP-1 concentration (top row) and PEG28-PD-1 concentrations (bottom row) with linear regression (red line; R^2 and p-values without corrections). Red asterisks denote significant correlations at 5% level for Bonferroni-corrected p-values. Averages and SEMs of fitted parameters are shown in boxes above corresponding plots (n=14). All parameters are summarised in Table S1.

Isolating the molecular reach of SHP-1 by varying the tether length

The molecular reach of the reaction, $L = (\sigma^*)^{-1/3}$, determined using the SPR-based assay involves two components: the reach of the PEG-peptide tether and the reach of the enzyme. As the reach contributed by the tether is progressively decreased (e.g. by using progressively shorter tethers), eventually the molecular reach of the reaction will be wholly determined by the reach of the enzyme. Indeed, if we assume that the reach of the tethers and enzyme can be effectively modelled by worm-like chains, an equation can be derived to relate L with the contour length of the tether (Eq. 4, see Methods). This model predicts that the squared molecular reach of the reaction should be linearly related to the length of the tether (Eq. 5), with the reach of the enzyme being the vertical intercept (i.e. when the tether length is nil).

Therefore, we performed the SPR-based assay using a different number of PEG repeats (N_{PEG} = 0, 3, 6, 12, 28) coupled to the same short PD-1 ITSM peptide (Fig. 3A). As before, the extended MPDPDE model was able to fit the data and produced binding and catalysis parameters that were similar for different length PEG linkers with the exception of σ^*, which progressively increased as the number of PEG linkers were reduced (Fig. 3B). This is expected because with shorter PEG linkers the local volume that SHP-1 is confined to decreases, thereby increasing local concentration.

As expected, the squared molecular reach of the reaction (determined by converting σ^* to L) increased with the number of PEG linkers (Fig. 3C). Using regression, we determined the vertical intercept, and hence the molecular reach of SHP-1, to be $L_{\text{SHP-1}} = 13.0$ nm. This value is between estimates obtained using crystal structure and maximum stretch (Fig. 1B).

We also performed experiments in which the PD-1 peptide is directly coupled to the surface without any PEG linkers. In Fig. 3C, this is labeled PEG0 and produced a molecular reach of 10.9±0.3 nm. Although this value is also within theoretical estimates and similar to the value obtained by the intercept method above (Fig. 1B), we reasoned that it may be less accurate because this very short peptide can introduce steric hindrance to binding and catalysis, which is reflected in the larger value of K_{D} and smaller value of $k_{\text{cat}}(\text{solution})$ that this peptide produces compared to peptides with PEG linkers, and this was also noted in our previous work (12).

PD-1 contributes less than SHP-1 to the molecular reach of the reaction

Given that the molecular reach of the reaction is determined by both the enzyme and tether, we next sought to directly determine the molecular reach of the cytoplasmic tail of the surface receptor. We injected SHP-1 over immobilised peptide corresponding to the cytoplasmic tail of PD-1 from the membrane to the ITSM. This N-terminally biotinylated peptide contained 64 aa with the phosphorylated tyrosine in the ITSM being 55 aa from the membrane (position 248 in the native sequence). The extended MPDPDE model was fit to the SPR traces (Fig. 4A) and provided estimates of the biophysical parameters (Fig. 4B).

Using the value of σ^*, we calculated the combined molecular reach of the reaction for PD-1-bound SHP-1 acting on PD-1 to be 16 nm. Given that we already obtained an estimate for the reach of SHP-1, we were able to back calculate the reach of PD-1 (see Eq. 4) to be 6.55 nm (Fig. 4C). Thus, we find that PD-1 contributes less to the overall molecular reach of the reactions compared to the SHP-1 reach contribution of 13.0 nm.

We note that the worm-like-chain model would predict a 3.0 nm reach for the PD-1 peptide we have used

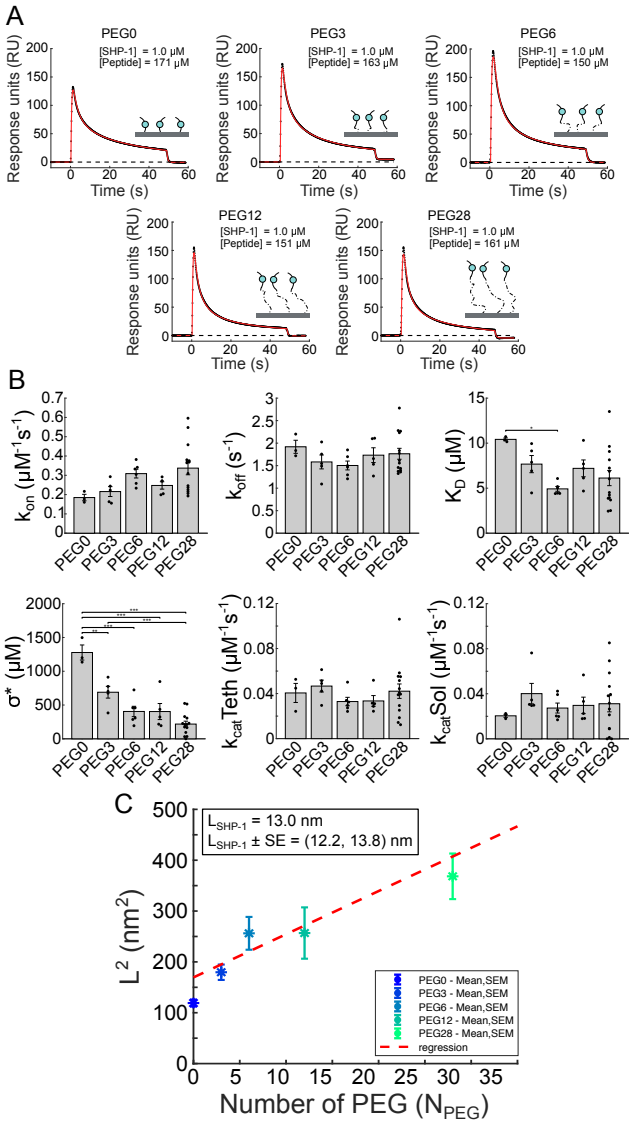

Figure 3: **Isolating the molecular reach of SHP-1 by varying PEG-PD-1 tether lengths.** (A) Representative SPR traces (black dots) and extended MPDPDE model fits (red lines) for the indicated number of PEG linkers (N_{PEG} =0, 3, 6, 12, 28). (B) Averages and SEMs for fitted parameters at indicated PEG linker length. Individual data points are plotted as black dots. Pairwise multiple t-test of parameters and PEG lengths shown for (*) 0.05, (**) 0.01, and (***) 0.001 significance. Significant differences are largely observed for σ^*, which determines the molecular reach of the reaction ($L = (\sigma^*)^{-1/3}$). All parameters are summarised in Table S1. (C) Average squared molecular reach of reaction plotted against number of PEG linkers. Red dashed line indicates regression (p-value = 10^{-11}; see Methods). The indicated molecular reach of SHP-1 is estimated by the vertical intercept using the regression line.

assuming a persistence length of 0.4 nm that applies to random amino acid chains (17, 27). Therefore, the experimentally measured reach of PD-1 appears to be twice that predicted by the worm-like-chain model, suggesting a preference for extended conformations of this peptide.

The binding affinity between SHP-1 and singly phosphorylated PD-1 was determined to be 11±2 μM.

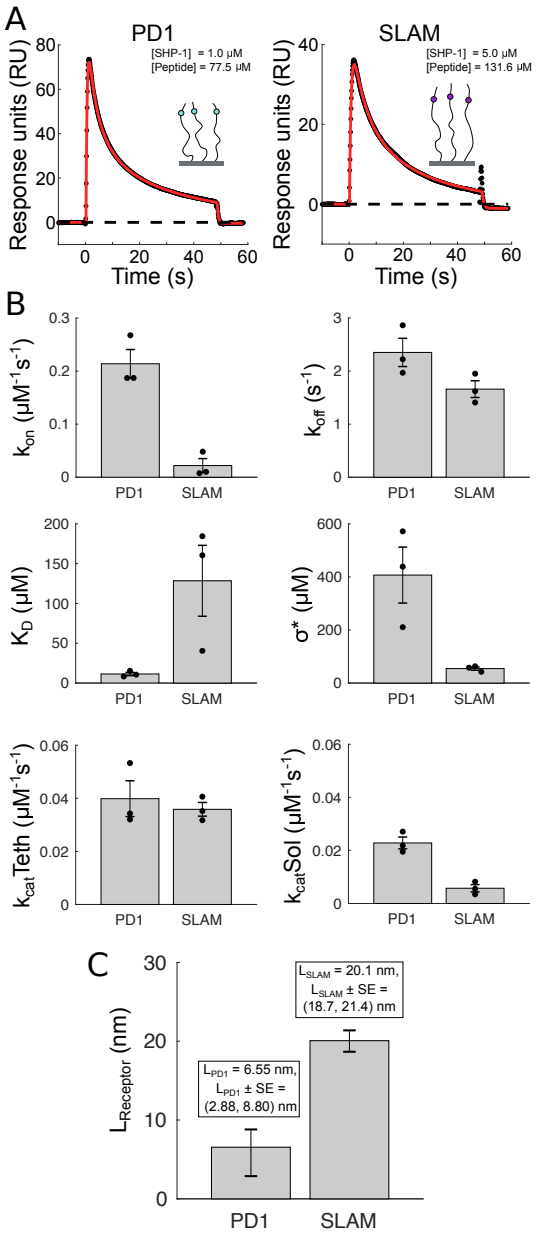

Figure 4: **Contribution of PD-1 and SLAM cytoplasmic tails to the molecular reach of the reaction.** (A) Representative SPR traces (black dots) and extended MPDPDE model fits (red lines) for the singly phosphorylated PD-1 (55 aa to phosphorylated tyrosine) and SLAM (69 aa to phosphorylated tyrosine) peptides. (B) Averages and SEMs for fitted parameters. Individual data points plotted as black dots. PD-1 exhibits a larger local concentration (σ^*) consistent with a shorter molecular reach. All parameters are summarised in Table S1. (C) Average molecular reach (±SE) for PD-1 and SLAM calculated by parsing out the reach of SHP-1 using $L_{\text{PD-1 or SLAM}} = ((L^2 - L^2_{\text{SHP-1}})/2)^{1/2}$, where L is the molecular reach of the reaction calculated from σ^* in panel B and $L_{\text{SHP-1}}$ = 13.0 nm.

Using a different assay, Hui et al (5) reported an affinity of 4.28 μM. The 2.5-fold higher affinity they report may be a result of using doubly phosphorylated PD-1 peptides.

The ratio of $k_{\text{cat}}(\text{tethered})$ to $k_{\text{cat}}(\text{solution})$ provides an estimate for the strength of allosteric activation of SHP-1 upon SH2-domain binding to PD-1. We find a modest 2-fold increase in activity from this effect (Fig. 4B). Since larger fold increases have been reported previously (9, 10, 12), we further explored this finding. First, we used a standard solution assay whereby SHP-1 acted on a low molecular weight synthetic substrate and confirmed that catalytic activity increased only 2-fold upon addition of a phosphorylated PD-1 peptide (Fig. S4). Second, we previously reported a larger allosteric activation for murine SHP-1 binding to the inhibitory receptor LAIR-1 but at 10°C and therefore performed experiments at this lower temperature, finding again only a modest increase in activity (Fig. S5). We conclude that human SHP-1 exhibits only modest allosteric activation upon binding to singly phosphorylated PD-1.

As a positive control to ensure our SPR-based assay is sensitive to reach, we repeated the experiments using the longer cytoplasmic tail of signalling lymphocyte activation molecule (SLAM), a surface receptor that is also known to recruit SHP-1 (29). The N-terminally biotinylated peptide contained 77 aa with the phosphorylated tyrosine in the ITSM being 69 aa from the membrane (position 327 in the native sequence). Performing the analysis as for PD-1, we find that the molecular reach contributed by SLAM is 20 nm (Fig. 4). This is markedly more than the reach of SHP-1 and comprises 72% of the predicted contour length for the SLAM peptide ($l_c \sim 69 \cdot 0.4\,\text{nm} = 27.6\,\text{nm}$). This suggests that SLAM has a larger persistence length than would be expected for random amino acids and/or is otherwise biased towards extended conformations.

Interestingly, we observed a larger 6.2-fold allosteric activation for SHP-1 interacting with SLAM (Fig. 4B) and this is highlighted when plotting the ratio of $k_{\text{cat}}(\text{tethered})$ to $k_{\text{cat}}(\text{solution})$ across all experimental conditions (Fig. S6). However, this allosteric activation for SLAM was a result of a lower $k_{\text{cat}}(\text{solution})$, not a higher $k_{\text{cat}}(\text{tethered})$, compared to PD-1. We also observe a much smaller on-rate for SHP-1 binding to SLAM compared to PD-1. A possible explanation for both observations is that the SLAM peptide may have fewer configurations in which the phosphotyrosine is available for interaction with SHP-1 when in solution.

Control of surface receptor signalling by the molecular reach of SHP-1

We next used a mathematical model to explore the impact of the measured molecular reach on surface receptor signalling at the membrane (Fig. 5A). Using the measured reach of PD-1 and SHP-1, we calculated their combined reach as 14.6 nm ($\sqrt{L^2_{\text{PD-1}} + L^2_{\text{SHP-1}}}$) combined reach as 14.6 nm. Using this number, we first consider the effective concentration of the SHP-1 catalytic domain that a substrate would experience when SHP-1 is tethered to PD-1 and PD-1 is randomly distributed on the membrane. We find that at physiological densities of PD-1, this effective concentration is $\sim 1000\ \mu$M (Fig. 5B,C), which is $\sim$1000-fold larger than the $\sim 1\ \mu$M concentration of SHP-1 in the cytosol assuming it is uniformly distributed (12, 30).

For tethered reactions, even though the effective concentration can be large, the coverage can in principle be low because a random or uniform distribution of surface receptors can allow some substrates to be out of reach (Fig. 5A). We therefore calculate the fraction of substrates that can be accessed by SHP-1 bound to PD-1 for different values of the molecular reach of the reaction and PD-1 density (Fig. 5E,F). If PD-1/SHP-1 complexes are uniformly distributed on the cell surface, we estimate that they are only able to achieve a moderate $\sim 15\%$ coverage of the substrates (Fig. 5E,F). Clustering of PD-1 with its substrates, which has been experimentally observed (5, 19), would lead to a higher local density and could therefore be important to improve both the effective concentration and coverage. A clustered density of $0.0034\,\text{nm}^{-2}$ (about 10-fold higher than a uniform estimate) is required to achieve a 90% coverage.

We next explored the contribution of the substrate reach to both concentration and coverage. Previously, we noted that the number of amino acids between the membrane and activating or inhibiting tyrosine motifs differed with a median of 33 aa (or 13 nm) or 65 aa (or 26 nm), respectively (12). We therefore repeated the calculations by increasing the contribution of the substrate reach from 0 nm (used in Fig. 5B,C,E,F) to a maximum of 30 nm and found a gradual increase in effective concentration (Fig. 5D) and coverage (Fig. 5G) with increasing substrate reach. Within this realistic range of substrate reaches and with uniform distributions, it was not possible to achieve high coverage (e.g. 90%), suggesting that PD-1 co-clustering with substrate is critical for effective inhibition.

Discussion

Using our extended SPR-based assay for tethered signalling reactions (12), we provide the first estimate of the molecular reach of SHP-1 to be 13.0 nm. This value is reasonable given that it is between an estimate from crystal structure of the open active conformation and an estimate assuming its linkers are maximally stretched (Fig. 1B). This has several implications for the mechanism of SHP-1 activity and the potency of inhibitory surface receptors.

The activity of SHP-1 is thought to be regulated by allosteric activation. This is supported by crystal structures showing both a closed autoinhibitory conformation, where the N-SH2 domain blocks the catalytic pocket (31), and an open conformation, where the N-SH2 is rotated, exposing the catalytic pocket (32). Interestingly, the molecular reach of SHP-1 that we report (13.0 nm) is substantially longer than the reach obtained from the open conformation structure (5.3 nm). This suggests that the functionally relevant state of SHP-1 is a spectrum of extended conformations, rather than the single open conformation observed in crystals, whereby inter-domain linkers allow SHP-1 to achieve a long molecular reach.

The reported magnitude of allosteric activation for SHP-1 upon SH2 domain binding has ranged from 2- to 20-fold (9, 10, 12). Here, we found a 2-fold increase in catalytic activity for PD-1 in both the SPR assay (Table S1, Fig. S6) and a solution assay (Fig. S4). This fold increase is much smaller than the $\sim$1000-fold increase in effective SHP-1 concentration experienced by membrane substrates when it moves from the cytosol to the membrane (Fig. 5C). Given that both allosteric activation and local concentration mechanisms critically rely on SH2 domain binding, it follows that both contribute to controlling SHP-1 activity.

Recent reports have suggested that allosteric activation of SHP-2 requires simultaneous binding of both SH2 domains on the same (14) or across different PD-1 peptides (13). Although SHP-1 in our assay could in principle bind across two PD-1 peptides, the observed fast kinetics and low affinity (Fig. 4) were characteristic of single SH2 domain binding and not high affinity tandem SH2 binding, as for example observed for ZAP-70 and Syk in SPR (33, 34). A possible explanation for this discrepancy is that SHP-1 exhibits high catalytic activity so that it dephosphorylates nearby peptides before SH2 domains are able to engage. If this is the case, it suggests that SHP-1 activity may need to be regulated on the membrane to avoid this negative feedback, and this regulation may involve its interactions with Themis (35–37).

The measured molecular reach for PD-1 and SLAM were larger than would be predicted based on the worm-like-chain model, indicating that both have a preference for extended conformations and that theoretical predictions may not accurately predict reach. It will be important to investigate additional immune receptors to determine whether extended conformations are widely observed and to compare the reach values with direct measurements in relevant cells (e.g. T cells) in the future. Discrepancies between measurements

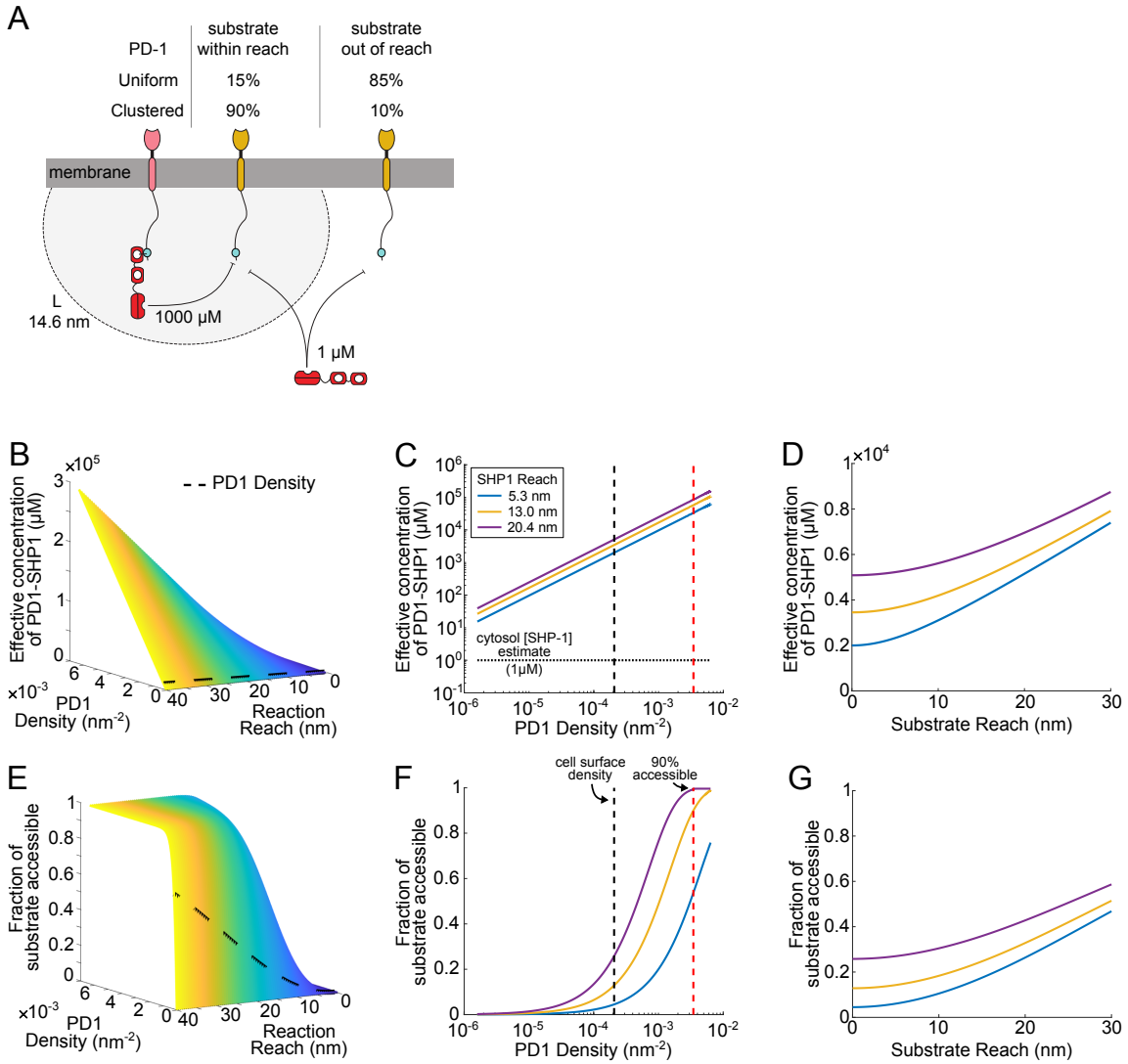

Figure 5: **Tethering of SHP-1 to PD-1 generates high membrane concentrations but poor coverage unless PD-1 co-clusters with substrates.** (A) Schematic of SHP-1 reactions with substrates, demonstrating tethered reaction (left SHP-1 molecule) and solution reaction (right SHP-1 molecule). (B-D) Effective concentration of PD-1–SHP-1 complex experienced by a substrate and (E-G) fraction of substrate within reach by PD-1–SHP-1 complexes under different conditions: (B,E) Versus the molecular reach of reaction and the density of PD-1–SHP-1 complex on the membrane. The cell surface PD-1–SHP-1 density estimate is shown with black dashed line. (C,F) Versus PD-1–SHP-1 density for different estimates of SHP-1 molecular reach, and fixed PD-1 and substrate molecular reach (6.55 nm and 0 nm, respectively). The cell surface PD-1–SHP-1 density estimate is shown with black dashed line. Density required for 90% substrate accessibility (0.0034 nm^{-2}) is shown with red dotted line. Estimate of cytosol SHP-1 concentration (1 μM) is shown with dotted line in C. (D,G) Versus substrate reach (for fixed reach of PD-1 and indicated reach of SHP-1) and PD-1–SHP-1 density ($\sim 2 \cdot 10^{-4}\,\text{nm}^{-2}$). Coloured lines in C,D,F,G refer to the theoretical and experimental estimates of the molecular reach of SHP-1 (Fig. 1B), see legend in C.

could point to additional regulation mechanisms operating *in vivo*, such as the reported associations between some immune receptor tails and the plasma membrane (38–41), which are not captured in our *in vitro* assays.

The biophysics of reactions between molecules on surfaces are more complex than in 3D bulk because, for example, there is no well-defined diffusion-limited reaction rate (42, 43) and rebinding is significant (44–51). This has led to discussion about the validity of different modeling approaches (52) (let alone computational approaches to study these models (53)), for example whether to assume Doi-type or first-passage-type reactions. Our work provides a specific instance where a detailed, molecular-scale model has been successfully deployed and validated with systematically controlled experiments. The model assumes a separation of timescales (16) between the fast motion of the tether as it explores its local probability density cloud (Eq. 2), and a reaction rate proportional to local 3D concentrations ($k_{\mathrm{cat}}(\mathrm{tethered})$, which has units of $\mu\mathrm{M}^{-1}\mathrm{s}^{-1}$). This experimentally validated model can be coupled to surface diffusion (16) and, in the future, other biophysical phenomena.

The potency of immune receptor reactions is controlled by many factors, including the efficiency of their phosphorylation and the affinity and catalytic activity of their recruited enzyme effectors (54–58). The molecular reach of the tethered enzyme also controls potency but is often overlooked because it has been difficult to experimentally measure and incorporate into mathematical models. Using a mathematical model coupled to reach measurements, we show how reach of the receptor and enzyme contributes to the potency of an inhibitory immune receptor. The work suggests the possibility of molecular reach inhibitors that need not target conserved catalytic pockets but are nonetheless able to control receptor potency.

Methods

SHP-1 molecular reach estimates from structure

Using the structure of SHP-1 in the open conformation (PDB 3PS5) and sequence data from UniProt (P29350), we can estimate a range of reach values for SHP-1. Direct measurement from PDB structure of N-SH2 binding site to catalytic site gives a reach estimate of 5.3 nm. For our maximum reach estimate, we subdivide SHP-1 into 3 structured domains (N-SH2, C-SH2, PTP) and 2 linker domains. For the structured domains, distances were measured from the structure in PDB 3PS5: between binding pocket and linker for N-SH2, between two linkers for C-SH2, and from the linker to the active site for PTP. We then count the number of residues in the two intervening disordered linker domains, and compute contour length assuming these are fully extended. Adding these 5 numbers together (N-SH2, linker, C-SH2, linker, PTP) yields a value $20.4\,\mathrm{nm}$. All measurements of structured domains were calculated using the measurement tool in PyMol.

Peptides and SHP-1

All phosphopeptides were custom-synthesized by Peptide Protein Research, Ltd. and were N-terminally biotinylated. Peptide sequences are listed in Table 1. Human SHP-1 with an N-terminal 6x His tag was produced in *Escherichia coli* BL21-CodonPlus (DE3)-RIPL strain (Agilent Technologies) and purified on Ni^{2+}-NTA agarose (Invitrogen) (12). Aliquots were stored at -80°C. On the day of experiment, SHP-1 was further purified by size-exclusion chromatography on an AKTA fast protein liquid chromatography system

equipped with a Superdex S200 10/300 GL column (both from GE Healthcare Life Sciences) equilibrated with 10 mM Hepes (pH 7.4), 150 mM NaCl, 3 mM EDTA, 0.05% Tween 20 supplemented with 1 mM dithiothreitol. SHP-1 concentration was determined from absorbance at 280 nm measured on a Nanodrop ND-2000 spectrophotometer (Thermo Scientific).

Table 1: Peptides used in this study (phosphotyrosines are denoted as Y*)

Name	Sequence
PEG28-PD-1	biotin–$(PEG)_{28}$–SVPEQTEY*ATIVFPSG
PEG12-PD-1	biotin–$(PEG)_{12}$–SVPEQTEY*ATIVFPSG
PEG6-PD-1	biotin–$(PEG)_{6}$–SVPEQTEY*ATIVFPSG
PEG3-PD-1	biotin–$(PEG)_{3}$–SVPEQTEY*ATIVFPSG
PEG0-PD-1	biotin–SVPEQTEY*ATIVFPSG
PD-1	biotin–SRAARGTIGARRTGQPLKEDPSAVPVFSVDYGELDFQ WREKTPEPPVPSVPEQTEY*ATIVFPSG
SLAM	biotin–QLRRRGKTNHYQTTVEKKSLTIYAQVQKPGPLQKKLD SFPAQDPCTTIYVAATEPVPESVQETNSITVY*ASVTLPES

Surface Plasmon Resonance

Experiments were performed on a Biacore T200 instrument (GE Healthcare Life Sciences) at 37°C and a flow rate of 10 μl/min. Running buffer was the same as for size-exclusion chromatography. Streptavidin was coupled to a CM5 sensor chip using an amino coupling kit to near saturation, typically 10000–12000 response units (RU). Biotinylated peptides were injected into the experimental flow cells (FCs) for different lengths of time to produce desired immobilisation levels (typically 25–100 RU). Concentrations of immobilized peptides were determined from the RU values as described in (12). The molar ratio of peptide to streptavidin was kept below 0.25 to avoid generating streptavidin complexes with more than 1 peptide. Usually, FC1 and FC3 were used as references for FC2 and FC4, respectively. Excess streptavidin was blocked with biotin (Avidity). Before SHP-1 injection, the chip surface was conditioned with 10 injections of the running buffer and SHP-1 was then injected over all FCs; the duration of injections was the same for conditioning and SHP-1 injection (45 s).

Solution assay for allosteric activation of SHP-1

The reaction mixture contained (final concentrations) 80 mM HEPES (pH 7.4), 1 mM DTT, 60 μM PEG0-PD-1 peptide, 5% DMSO (vehicle), 10 mM p-nitrophenyl phosphate (*p*NPP), and 0.1 μM SHP-1; the reaction was started by adding SHP-1. The reaction mixtures were incubated at 37°C. Aliquots were withdrawn at appropriate time points and dephosphorylation was stopped by addition of an equal volume of freshly prepared 80 mM HEPES (pH 7.4), 20 mM iodoacetamide, 100 mM Na_3VO_4. Absorbance at 405 nm was measured on the Nanodrop ND-2000. In the control, the quenching solution was added before SHP-1 and the mixture was kept either on ice or at 37°C for the duration of the time course. The efficiency of quenching was confirmed by the absence of a difference in absorbance between samples kept on ice or at 37°C.

MPDPDE model and parameter fitting

We modified our previously reported multicenter particle density partial differential equation (MPDPDE) model (12). The original model included five fitting parameters (labelled p_1 to p_5) that are used to recover the five biophysical parameters: binding and unbinding rates k_{on}, k_{off} of the enzyme to the receptor, the catalytic rate of the enzyme in solution $k_{\text{cat}}(\text{solution})$, the catalytic rate of the enzyme when tethered to the receptor $k_{\text{cat}}(\text{tethered})$, and the effective local concentration σ^* or equivalently, molecular reach of the reaction L. The present data exhibited nonspecific binding of the enzyme to the surface that differed in magnitude between the control and experimental flow cells and as a result, produced a different baseline before and after the SHP-1 injection. We modified the original model to include non-specific binding with rate n_{ns} that changed linearly with time (see Fig. S2) between the start (p_{start}) and end (p_{end}) of the SHP-1 injection. Therefore, the extended model included 3 additional fitted parameters compared to the original model (12).

To fit the SPR data to the extended MPDPDE model, we use a simulated annealing algorithm (59), with at least 10^5 steps and a temperature function decreasing to zero as $\left(1-\left([\text{step}]/10^5\right)^4\right)$. For initial guess, we used

$$k_{\text{on}} = 0.1\,\mu\text{M}^{-1}s^{-1}, L = 14.5\text{nm}, k_{\text{cat}}(\text{tethered}) = 0.01\,\mu\text{M}^{-1}\text{s}^{-1}, \text{k}_{\text{cat}}(\text{solution}) = 0.002\,\mu\text{M}^{-1}\text{s}^{-1}.$$

For the initial guess of k_{off}, we first fit an exponential curve to the SPR time series data in the dissociation phase after SHP-1 injection ceases (e.g., after $t = 45$s in Fig. 2A). We find the parameters generated by simulated annealing are in close agreement with parameters found from MATLAB's least-squares curve fitting (lsqcurvefit) function (not shown). However, the sum of square error for the parameters found using simulated annealing is consistently smaller. We perform simulated annealing three times on each dataset, using the fit with the lowest sum of square error for our analysis. To test for under-constrained parameter fitting, we perform a Markov Chain Monte Carlo (59) with unbounded, flat priors for each parameter. The resulting posteriors show that the parameters can be independently determined (Fig. S3). All model evaluation and fitting are implemented in MATLAB 2017b.

Estimation of molecular reach

The molecular reach of the reaction, L, in our SPR assays is influenced by the reach for the tether, L_{tether}, and the reach of the enzyme, $L_{\text{SHP-1}}$. For a worm-like chain model, the probability density of a site on the molecule at location $\vec{x}$ is

$$P(\vec{x}; L_{\text{X}}) = \left(\frac{3}{2\pi L^2}\right)^{3/2} \exp\left(-\frac{3\vec{x}\cdot\vec{x}}{2L^2}\right) \tag{1}$$

where L_{X} is a property of the molecule. For a worm-like chain model, $L_{\text{X}} = \sqrt{2l_c l_p}$, where l_c is the contour length and l_p is the persistence length, but we note that Eq. 1 arises in more general molecular models, so we use it to describe the behavior of the enzyme, without the interpretation of L_{X} in terms of a contour length and persistence length. In (12), we show that this leads to a local concentration kernel

$$\sigma(r) = \left(\frac{3}{2\pi L^2}\right)^{3/2} \exp\left(-\frac{3r^2}{2L^2}\right) \tag{2}$$

where r is the distance between the anchors of the two tethers, and

$$L = \sqrt{L_{\text{tether}}^2 + L_{\text{tether}}^2 + L_{\text{SHP-1}}^2} \tag{3}$$

$$= \sqrt{2 \cdot L_{\text{tether}}^2 + L_{\text{SHP-1}}^2}. \tag{4}$$

For disordered domains and PEG linkers, we interpret L in terms of the worm-like chain model (17, 18), so the reach can be estimated from the contour length and the persistence length of the domain. For the constructed PEG-PD-1 peptides, the contour length (from the surface anchor to binding site of SHP-1) is the number of PEG linkers N_{PEG} times the length of a single PEG, $l_{\text{PEG}} \sim 0.4\,\text{nm}$ (60). From this, we derive an approximation for the reach of SHP-1,

$$L^2 = 4 \cdot N_{\text{PEG}} \cdot l_{\text{PEG}} \cdot l_p + L_{\text{SHP-1}}^2, \tag{5}$$

predicting that the reach is given by the intercept of the line L^2 versus N_{PEG}.

Uncertainty quantification for derived parameters

For each PEG length, L^2 is calculated by averaging the fitted parameter σ^* for all replicates and transforming the average to a single L^2 value for the peptide. Error propagation is used to convert the standard deviation of σ^* to an error for L^2.

Best fit lines with associated R-values and p-values for PEG28-PD1 parameters versus phosphatase and peptide concentrations, shown in Fig. 2 and 3 were determined using MATLAB's robust fitlm function.

We use MATLAB's anova1 and multcompare functions to conduct multiple comparison t-tests on paired PEG peptide parameters to establish significant differences. Pairs that are significantly different at the 0.05, 0.01, and 0.001 level are shown.

Implications of reach for reactions at the cell membrane

If PD-1 is uniformly distributed on the cell, we estimate its surface density ρ_0 by assuming 65,000 PD-1 molecules per T cell (61) and assuming that the T cell is approximately a sphere of radius $5\,\mu$m, giving a PD-1 surface density of $\sim 2 \cdot 10^{-4}\,\text{nm}^{-2}$. We use $1\,\mu$M as the concentration of cytosolic SHP-1 (61). The effective concentration experienced by a substrate is then given by

$$C_{\text{eff}} = \iint \sigma(r)\rho_0 dA \tag{6}$$

$$= \left(\frac{3}{2\pi}\right)^3 \frac{\rho_0}{L_{\text{rxn}}} \tag{7}$$

Since tethered reactions are heterogeneously distributed on the membrane, some substrate molecules are inaccessible to the enzyme. We determine what fraction of the substrate is accessible by a PD-1–SHP1 complex for a given reach of reaction and PD-1 density. To do this, we calculate the probability of at least one PD-1–SHP1 complex being within a circle of radius L, of any given substrate. We assume finding a number of activated, SHP-1-bound PD-1 molecules within a disk around the substrate is Poisson distributed,

with $\lambda = \pi\rho_0 L_{\text{rxn}}^2$ and ρ_0 estimated above. We use this to determine the probability of at least one PD-1–SHP1 complex within reach,

$$P_{\geq 1} = 1 - \exp\left(-\pi\rho_0 L_{\text{rxn}}\right). \tag{8}$$

Acknowledgements

We thank Marion H. Brown, P. Anton van der Merwe, and members of the van der Merwe and Dushek laboratories for helpful discussions. The work has been funded by NSF CAREER grant (DMS 1454739 to JA), NSF grant DMS 1763272 for funding JA and LC and a grant from the Simons Foundation (594598, QN) for funding JA and LC, and a Wellcome Trust Senior Research Fellowship (207537/Z/17/Z to OD).

References

1. Chen L, Flies DB (2013) Molecular mechanisms of T cell co-stimulation and co-inhibition. *Nature reviews. Immunology* 13:227–42.

2. Long EO, Sik Kim H, Liu D, Peterson ME, Rajagopalan S (2013) Controlling Natural Killer Cell Responses: Integration of Signals for Activation and Inhibition. *Annual Review of Immunology* 31:227–258.

3. Dushek O, Goyette J, van der Merwe PA (2012) Non-catalytic Tyrosine Phosphorylated Receptors. *Immunological Reviews* 250:258–276.

4. Schildberg FA, et al. (2016) Coinhibitory Pathways in the B7-CD28 Ligand-Receptor Family. *Immunity* 44:955–972.

5. Hui E, et al. (2017) T cell costimulatory receptor CD28 is a primary target for PD-1-mediated inhibition. *Science* 355:1428–1433.

6. Celis-Gutierrez J, et al. (2019) Quantitative Interactomics in Primary T Cells Provides a Rationale for Concomitant PD-1 and BTLA Coinhibitor Blockade in Cancer Immunotherapy. *Cell Reports* 27:3315–3330.e7.

7. Xu X, et al. (2019) BTLA and PD-1 employ distinct phosphatases to differentially repress T cell signaling. *bioRxiv* p 669812.

8. Chemnitz JM, Parry RV, Nichols KE, June CH, Riley JL (2004) SHP-1 and SHP-2 Associate with Immunoreceptor Tyrosine-Based Switch Motif of Programmed Death 1 upon Primary Human T Cell Stimulation, but Only Receptor Ligation Prevents T Cell Activation. *The Journal of Immunology* 173:945–954.

9. Pei D, Wang J, Walsh CT (1996) Differential functions of the two Src homology 2 domains in protein tyrosine phosphatase SH-PTP1. *Proceedings of the National Academy of Sciences of the United States of America* 93:1141–1145.

10. Pei D, Lorenz U, Klingmüller U, Neel BG, Walsh CT (1994) Intramolecular Regulation of Protein Tyrosine Phosphatase SH-PTP1: A New Function for Src Homology 2 Domains. *Biochemistry* 33:15483–15493.

11. Chen YNP, et al. (2016) Allosteric inhibition of SHP2 phosphatase inhibits cancers driven by receptor tyrosine kinases. *Nature* 2:1–17.

12. Goyette J, et al. (2017) Biophysical assay for tethered signaling reactions reveals tether-controlled activity for the phosphatase SHP-1. *Science Advances* 3.

13. Patsoukis N, et al. (2020) Interaction of SHP-2 SH2 domains with PD-1 ITSM induces PD-1 dimerization and SHP-2 activation. *Communications Biology* 3:1–13.

14. Marasco M, et al. (2020) Molecular mechanism of SHP2 activation by PD-1 stimulation. *Science Advances* 6.

15. Pérez-Ferreros P, Gaus K, Goyette J (2019) Tethered signaling in inhibitory immune receptors. *Frontiers in Physics* 6:1–8.

16. Zhang Y, et al. (2019) The Influence of Molecular Reach and Diffusivity on the Efficacy of Membrane-Confined Reactions. *Biophysical Journal* 117:1189–1201.

17. Van Valen D, Haataja M, Phillips R (2009) Biochemistry on a leash: The roles of tether length and geometry in signal integration proteins. *Biophysical Journal* 96:1275–1292.

18. Bryant D, Clemens L, Allard J (2017) Computational simulation of formin-mediated actin polymerization predicts homologue-dependent mechanosensitivity. *Cytoskeleton* 74.

19. Yokosuka T, et al. (2012) Programmed cell death 1 forms negative costimulatory microclusters that directly inhibit T cell receptor signaling by recruiting phosphatase SHP2. *Journal of Experimental Medicine* 209:1201–1217.

20. Schamel WW, et al. (2005) Coexistence of multivalent and monovalent TCRs explains high sensitivity and wide range of response. *The Journal of Experimental Medicine* 202:493–503.

21. Yokosuka T, et al. (2005) Newly generated T cell receptor microclusters initiate and sustain T cell activation by recruitment of Zap70 and SLP-76. *Nature Immunology* 6:1253.

22. Goyette J, Gaus K (2017) Mechanisms of protein nanoscale clustering. *Current opinion in cell biology* 44:86–92.

23. Pageon SV, et al. (2013) Superresolution microscopy reveals nanometer-scale reorganization of inhibitory natural killer cell receptors upon activation of NKG2D. *Science signaling* 6:ra62.

24. Garcia-Parajo MF, Cambi A, Torreno-Pina JA, Thompson N, Jacobson K (2014) Nanoclustering as a dominant feature of plasma membrane organization. *Journal of Cell Science* 127:4995–5005.

25. Lopes FB, et al. (2017) Membrane nanoclusters of FcγRI segregate from inhibitory SIRPα upon activation of human macrophages. *The Journal of Cell Biology* p jcb.201608094.

26. Suter EC, Schmid EM, Voets E, Francica B, Fletcher DA (2020) Antibody:CD47 ratio regulates macrophage phagocytosis through competitive receptor phosphorylation. *bioRxiv* pp 1–62.

27. Zhou H (2001) Loops in proteins can be modeled as worm-like chains. *The Journal of Physical Chemistry B* 105:6763–6766.

28. Wang W, et al. (2011) Crystal structure of human protein tyrosine phosphatase SHP-1 in the open conformation. *Journal of cellular biochemistry* 112:2062–71.

29. Cannons JL, Tangye SG, Schwartzberg PL (2011) SLAM family receptors and SAP adaptors in immunity. *Annual review of immunology* 29:665–705.

30. Hukelmann JL, et al. (2015) The cytotoxic T cell proteome and its shaping by the kinase mTOR. *Nature Immunology* 17.

31. Yang J, et al. (2003) Crystal Structure of Human Protein-tyrosine Phosphatase SHP-1. *Journal of Biological Chemistry* 278:6516–6520.

32. Wang W, et al. (2011) Crystal structure of human protein tyrosine phosphatase SHP-1 in the open conformation. *Journal of cellular biochemistry* 112:2062–71.

33. Hughes CE, et al. (2010) CLEC-2 activates Syk through dimerization. *Blood* 115:2947–55.

34. Goyette J, et al. (2020) Regulated unbinding of ZAP70 at the T cell receptor by kinetic avidity. *bioRxiv*.

35. Paster W, et al. (2015) A THEMIS:SHP1 complex promotes T-cell survival. *The EMBO journal* 34:393–409.

36. Choi S, et al. (2017) THEMIS enhances TCR signaling and enables positive selection by selective inhibition of the phosphatase SHP-1. *Nature Immunology* 18:433–441.

37. Brzostek J, et al. (2020) T cell receptor and cytokine signal integration in CD8+ T cells is mediated by the protein Themis. *Nature Immunology* 21:186–198.

38. Xu C, et al. (2008) Regulation of T cell receptor activation by dynamic membrane binding of the CD3epsilon cytoplasmic tyrosine-based motif. *Cell* 135:702–13.

39. Zhang H, Cordoba SP, Dushek O, Anton van der Merwe P (2011) Basic residues in the T-cell receptor ζ cytoplasmic domain mediate membrane association and modulate signaling. *Proceedings of the National Academy of Sciences of the United States of America* 108.

40. Dobbins J, et al. (2016) Binding of the cytoplasmic domain of CD28 to the plasma membrane inhibits Lck recruitment and signaling. *Science Signaling* 9:1–13.

41. Yang W, et al. (2017) Dynamic regulation of CD28 conformation and signaling by charged lipids and ions. *Nature Structural and Molecular Biology* 24:1081–1092.

42. Szabo A (1989) Theory of diffusion-influenced fluorescence quenching. *Journal of Physical Chemistry* 93:6929–6939.

43. Chew WX, et al. (2019) Surface reaction-diffusion kinetics on lattice at the microscopic scale. *Physical Review E* 99:42411.

44. Dushek O, Das R, Coombs D (2009) A role for rebinding in rapid and reliable T cell responses to antigen. *PLoS Computational Biology* 5.

45. Aleksic M, et al. (2010) Dependence of T cell antigen recognition on T cell receptor-peptide MHC confinement time. *Immunity* 32:163–74.

46. Govern CC, Paczosa MK, Chakraborty AK, Huseby ES (2010) Fast on-rates allow short dwell time ligands to activate T cells. *Proceedings of the National Academy of Sciences* 107:8724–9.

47. Dushek O, van der Merwe PA, Shahrezaei V (2011) Ultrasensitivity in multisite phosphorylation of membrane-anchored proteins. *Biophysical journal* 100:1189–97.

48. Abel SM, Roose JP, Groves JT, Weiss A, Chakraborty AK (2012) The membrane environment can promote or suppress bistability in cell signaling networks. *The journal of physical chemistry. B* 116:3630–40.

49. Mugler A, Bailey A, Takahashi K, Rein ten Wolde P (2012) Membrane Clustering and the Role of Rebinding in Biochemical Signaling. *Biophysical Journal* 102:1069–1078.

50. Dushek O, Van der Merwe PA (2014) An induced rebinding model of antigen discrimination. *Trends in Immunology* 35:153–158.

51. Lawley SD, Keener JP (2017) Rebinding in biochemical reactions on membranes. *Physical Biology* 14.

52. Agbanusi IC, Isaacson SA (2014) A Comparison of Bimolecular Reaction Models for Stochastic Reaction-Diffusion Systems. *Bulletin of Mathematical Biology* 76:922–946.

53. Schöneberg J, Ullrich A, Noë F (2014) Simulation tools for particle-based reaction-diffusion dynamics in continuous space. *BMC Biophysics* 7:1–10.

54. Mukhopadhyay H, Cordoba SP, Maini PK, van der Merwe PA, Dushek O (2013) Systems model of T cell receptor proximal signaling reveals emergent ultrasensitivity. *PLoS computational biology* 9:e1003004.

55. Hui E, Vale RD (2014) In vitro membrane reconstitution of the T-cell receptor proximal signaling network. *Nature Structural and Molecular Biology* 21:133–142.

56. Mukhopadhyay H, et al. (2016) Multisite phosphorylation of the T cell receptor z-chain modulates potency but not the switch-like response. *Biophys. J.* 110:1896–1906.

57. James JR (2018) Tuning ITAM multiplicity on T cell receptors can control potency and selectivity to ligand density. *Science Signaling* 11.

58. Courtney AH, et al. (2019) CD45 functions as a signaling gatekeeper in T cells. *Science signaling* 12.

59. Press WH, Teukolsky Sa, Vetterling WT, Flannery BP (2007) *Numerical Recipes 3rd Edition: The Art of Scientific Computing*.

60. Kienberger F, et al. (2000) Static and Dynamical Properties of Single Poly(Ethylene Glycol) Molecules Investigated by Force Spectroscopy. *Single Molecules* 1:123–128.

61. Hukelmann JL, et al. (2016) The cytotoxic T cell proteome and its shaping by the kinase mTOR. *Nature Immunology* 17:104–112.

Supplementary Information
Determination of the molecular reach of the protein tyrosine phosphatase SHP-1

Lara Clemens[1*], Mikhail Kutuzov[2*], Kristina Viktoria Bayer[2], Jesse Goyette[3,4], Jun Allard[1¶], Omer Dushek[2¶]

[1]Center for Complex Biological Systems, University of California Irvine, Irvine, CA 92697 USA
[2]Sir William Dunn School of Pathology, University of Oxford, OX1 3RE, Oxford, UK
[3]EMBL Australia Node in Single Molecule Science, School of Medical Sciences, University of New South Wales, Sydney 2052, Australia
[4]ARC Centre of Excellence in Advanced Molecular Imaging, University of New South Wales, Sydney 2052, Australia
[*]These authors contributed equally
[¶]Co-Corresponding authors

Table S1: Average biophysical parameter values for each peptide. All experiments conducted at temperature 37°C except where noted.

Substrate	N	k_{on} ($\mu\text{M}^{-1}s^{-1}$)	k_{off} (s^{-1})	K_{D} (μM)	L (nm)	σ^* (μM)	$k_{\text{cat}}(\text{tethered})$ ($\mu\text{M}^{-1}s^{-1}$)	$k_{\text{cat}}(\text{solution})$ ($\mu\text{M}^{-1}s^{-1}$)
PEG0	3	0.19 ± 0.02	1.9 ± 0.1	10.4 ± 0.2	10.9 ± 0.3	1300 ± 100	0.041 ± 0.008	0.020 ± 0.001
PEG3	5	0.22 ± 0.03	1.6 ± 0.2	8.0 ± 1.0	13.6 ± 0.7	690 ± 90	0.047 ± 0.005	0.040 ± 0.009
PEG6	6	0.31 ± 0.02	1.5 ± 0.1	4.9 ± 0.3	16.6 ± 1.0	410 ± 77	0.033 ± 0.004	0.027 ± 0.004
PEG12	5	0.25 ± 0.02	1.7 ± 0.2	7.2 ± 0.9	17.1 ± 1.0	400 ± 100	0.034 ± 0.005	0.030 ± 0.007
PEG28	14	0.34 ± 0.03	1.8 ± 0.2	6.1 ± 0.8	40 ± 15.0	210 ± 40	0.042 ± 0.006	0.031 ± 0.007
PEG28 (10°C)	8	0.28 ± 0.03	0.8 ± 0.06	2.9 ± 0.2	14 ± 1.0	960 ± 260	0.0036 ± 0.0006	0.0047 ± 0.0007
PD1	3	0.21 ± 0.03	2.4 ± 0.3	11.0 ± 2.0	17 ± 1.7	400 ± 100	0.040 ± 0.007	0.023 ± 0.002
SLAM	3	0.02 ± 0.01	1.7 ± 0.2	130 ± 40	31 ± 1.3	55 ± 6	0.036 ± 0.003	0.0058 ± 0.001

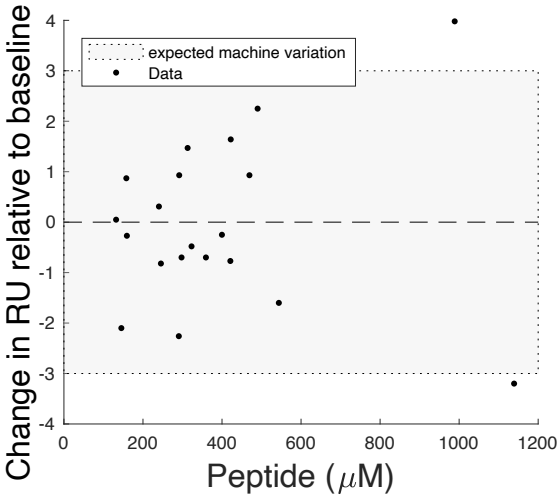

Figure S1: **Change in baseline before and after phosphatase injection is not correlated with phosphorylated peptide concentration.** The observed reduction in baseline RU after SHP-1 injection (see Fig. 2A,B) could be a result of the loss of phosphate mass from the chip surface. To investigate this possibility, alkaline phosphatase was injected over a surface immobilised with the indicated concentration of phosphorylated PEG28-PD-1 peptide for 300 seconds and the difference in baseline RU before and after injection was calculated. However, no correlation was observed with peptide concentration. The small $\sim$3 RU deviation is consistent with machine drift which is reported to be in the range of $\sim$1 RU per 100 seconds (gray area for our 300 second injection).

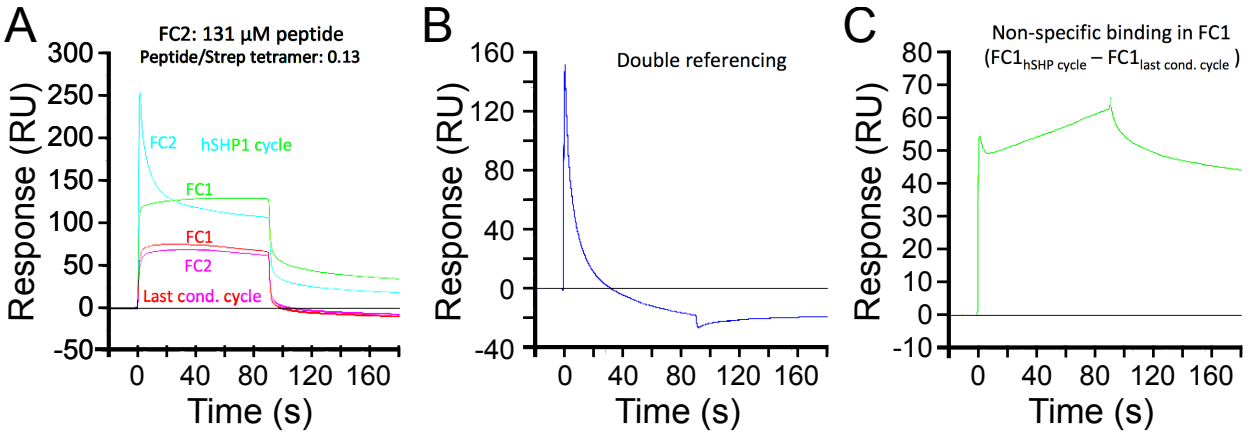

Figure S2: **Change in baseline before and after SHP-1 injection can be explained by non-specific SHP-1 binding.** (A) SPR traces of buffer injection (conditioning cycle) over flow cells 1 (red) and 2 (pink) followed by SHP-1 injection over flow cell 1 (green) and 2 (cyan). Flow cell 1 is a blank control whereas PEG28-PD-1 is immobilised in flow cell 2. All experiments were at at 37°C. Non-specific binding is apparent after SHP-1 injection because baseline remains above zero. (B) Double-referenced SPR trace for PEG28-PD-1 highlights a negative baseline after SHP-1 injection. This result suggests that non-specific binding in the control and experimental flow cells is not exactly matched. (C) Subtraction of the buffer injection from the SHP-1 injection in the control flow cell demonstrates that non-specific binding of SHP-1 can be approximated to be linear in time.

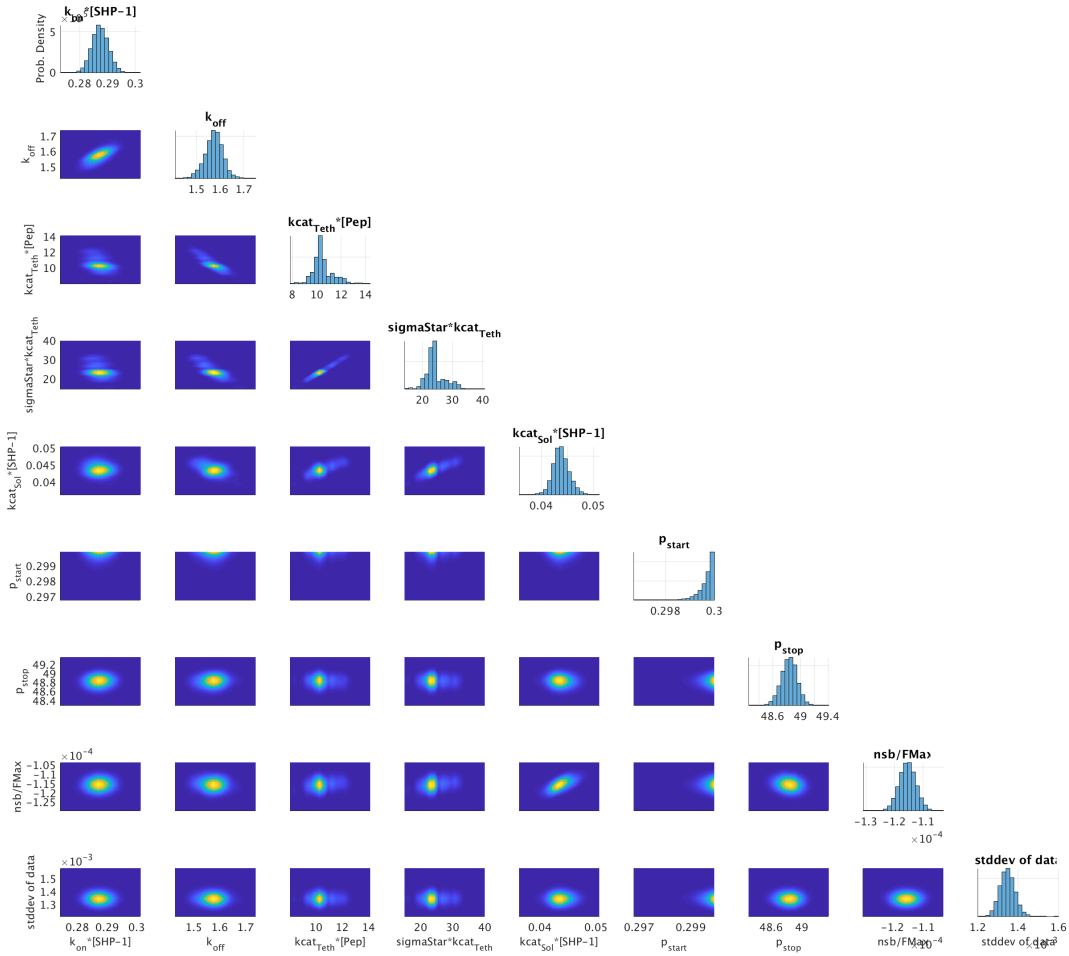

Figure S3: **Posterior distributions of individual fitted parameters.** Using Markov Chain Monte Carlo to fit the MPDPDE model to data obtained at 1 μM SHP-1 and 125 μM PEG28, demonstrates parameter estimates are well-identified.

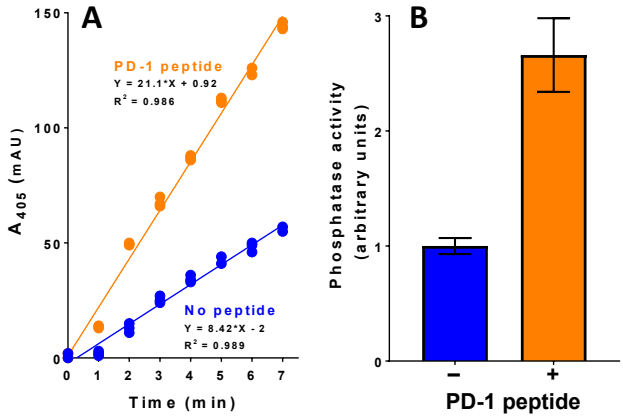

Figure S4: **Solution-based assay for SHP-1 catalytic activity confirms a modest allosteric activation by singly phosphorylated PD-1 peptide.** Human SHP-1 (0.1 μM) was incubated at 37°C with 10 mM pNPP in the absence (blue) or presence (orange) of 60 μM PEG0-PD-1 peptide. (A) Time course of pNPP dephosphorylation measured by absorbance at 405 nm at the indicated time points. Data points are technical replicates (n = 3). (B) The catalytic activity is determined by the fold-change in the slope of the time course data with a mean of 2.7. Error bars represent minimum and maximum from independent experiments (n=2).

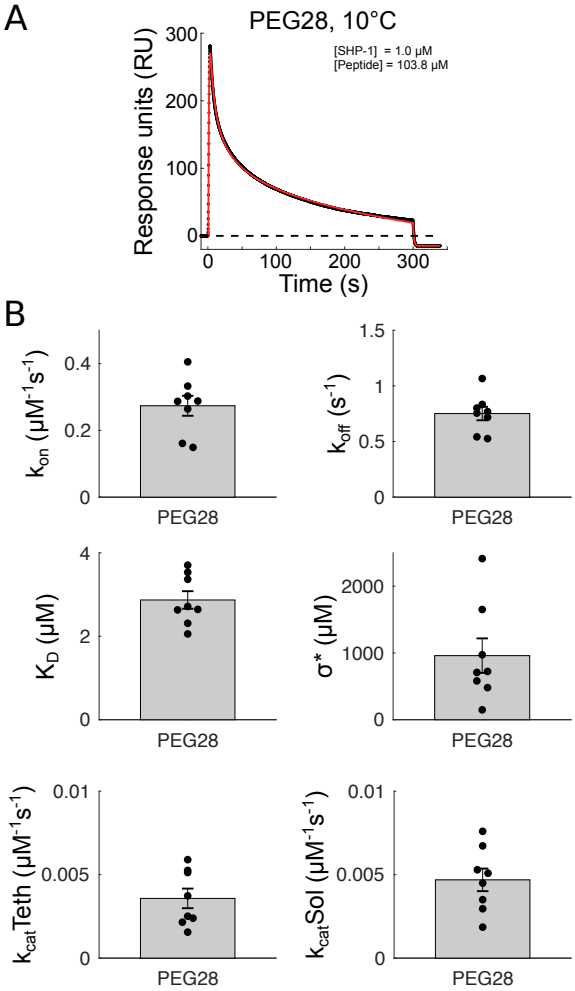

Figure S5: **SHP-1 injection over PEG28-PD-1 at 10°C.** (A) Representative SPR trace (black dots) and extended MPDPDE model fit (red line). (B) Averages and SEMs (gray with black error bars). Individual data points plotted as black dots.

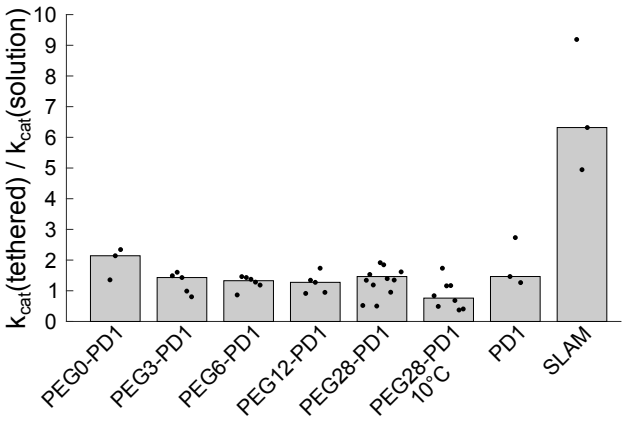

Figure S6: **Summary of $k_{\mathbf{cat}}$(tethered)/$k_{\mathbf{cat}}$(solution) for all experimental conditions.** Ratio of tethered to solution catalysis (k_{cat}(tethered)/k_{cat}(solution)) determined by SPR for the indicated conditions (all experiments at 37°C except where indicated). The median (gray bars) reveals only modest ∼1-2-fold allosteric activation for PD-1 across all conditions but a larger 6.2-fold activation for SLAM, which is discussed in the main text.